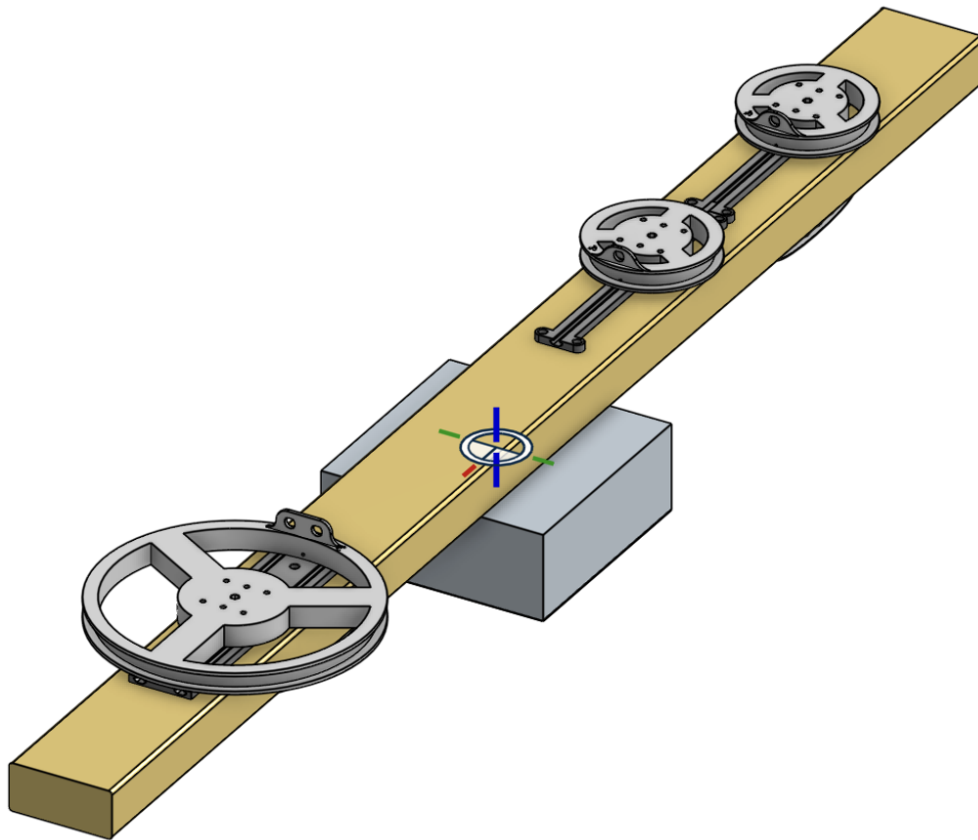


Geophysical Electromagnetic Scanner

Sabrina Ashik, Matthew Hasman, Tyler Wilson, Joel Tsuchitori

September 2024 to April 2025



Team 2459

ENPH 479

Engineering Physics Project Lab

The University of British Columbia

April 8, 2025

Executive Summary

The geophysical electromagnetic scanner is a multidisciplinary project that aims to address the global unexploded ordnance (UXO) problem. Each year, approximately 20,000 people are killed or injured due to UXOs UNICEF (2009). Detecting and removing UXOs is a significant challenge, requiring intelligent methods to wirelessly detect and classify underground objects. Traditional surveying tools, such as a metal detector, prove to be ineffective due to their inability to distinguish between UXOs and regular scrap metal. Therefore, tasked with this challenge, our team has partnered with a faculty advisor, Dr. Lindsey Heagy, professor in the UBC Department of Earth, Ocean, and Atmospheric Sciences, to address the global UXO problem.

Our team's objective is to create an electromagnetic device capable of collecting data in underground regions and then reconstructing an image of this underground region to classify objects as potential UXOs. Through this, our team developed a two-coil system capable of measuring the conductivity of subterranean materials. A two-coil system works by using the principles of electromagnetic induction—a primary transmitting coil emits a time-varying field, inducing eddy currents in underground materials, which induces a secondary field measured by a receiving coil. Our team explored the hardware and electronics necessary to optimize this device, along with software solutions to classify objects.

Through our progress, our team arrived at several key design takeaways to address this issue. The first takeaway was an innovative solution to be able to detect the secondary field in the presence of the much stronger primary field. Our design used a third bucking coil wired in series with the transmitting coil to create a third field, used to cancel the effects of the primary coil on the secondary coil. The second takeaway was our software pipeline that used a method known as geophysical inversion to invert raw data into a map of an underground region. This method relied on classical physics relations, but our team also saw promising results from machine learning diffusion models.

In conclusion, our team successfully designed an electromagnetic device capable of imaging and classifying underground objects as UXOs. Our team recommends that further progress on the topic of UXO classification fully explore novel solutions such as machine learning. Additionally, further miniaturization and ergonomics would give this device significant interest for various industry applications.

Contents

1	Introduction	1
2	Project Overview	1
2.1	Project Scope	1
2.2	Proposed Solution	2
3	Discussion	3
3.1	Hardware	3
3.1.1	Transmitting Coil	4
3.1.2	Receiving Coil	5
3.1.3	Bucking Coil	5
3.1.4	Mounting System	6
3.1.5	Coil Electrical Model	6
3.2	Circuitry	7
3.2.1	Transmitting Circuit	7
3.2.2	Receiving Circuit	8
3.3	Firmware	10
3.4	Dataset Acquisition	10
3.4.1	Motivation	10
3.4.2	Three-Loop Approximation	11
3.4.3	Multi-Loop Approximation	13
3.5	Geophysical Inversion	14
3.5.1	Inversion Algorithm Overview	14
3.5.2	Inversion Test Result	16
4	Conclusions	18
5	Recommendations	19
6	Deliverables	19
A	Circuit Schematics	20
A.1	Filter and Amplifier	20
A.2	Analog Phase Detection	21
A.3	Amplitude Detection	21
B	Microcontroller Selection	21

C	CAD of Coil Winding Holders	22
D	Physical Coil Parameters	24
E	Bucking Simulation	25
F	Forward Simulation Algorithms	26
F.1	Three-Loop Approximation Model	26
F.2	Multi-Loop Approximation	29
F.3	Dependence on Conductivity	30
G	Inversion Algorithm	31
G.1	Nonlinear Forward Model for Inversion	31
G.2	Inverse Problem Formulation	33
G.3	Regularization	33
G.4	Implementation Notes	34
	References	36

List of Figures

1	Physics overview of our proposed solution	2
2	Hardware system level diagram	3
3	Transmitting coil design	4
4	Receiving coil design	5
5	Bucking coil mounting system	5
6	Result of simulating bucking coil cancellation for various distances	6
7	LM1875 Audio Amplifier	7
8	Receiver circuit system-level diagram	8
9	The filtered and raw Rx signals.	8
10	Analog phase detection circuit.	9
11	System-level diagram for the firmware.	10
12	Field survey of a UXO response using a two-coil system	12
13	Diagram of the three-loop approximation model	12
14	Example of the primary-to-secondary field ratio using the three-loop approximation	13
15	Diagram of the multi-loop approximation model	13
16	Example of the primary-to-secondary field ratio using the multi-loop approximation	14
17	Iterative Inversion Workflow	15
18	Synthetic conductivity model with a cylindrical target	16

19	Reconstructed conductivity model after inversion and filtering	17
20	Inversion Result of Real Data	18
21	Schematic of a biquad filter.	20
22	Phase response of two biquad filters in series.	20
23	Schematic of analog phase detection circuit.	21
24	Schematic of amplitude detection circuit.	21
25	Bucking coil mounting arrangment	22
26	Carrying Handle	22
27	Electronics Box	23
28	Mounting Rail	23
29	Transmitting Coil	23
30	Recieving Coil	24
31	Full Assembly	24
32	Mutual induction between loops in the three-loop approximation.	27
33	Comparison of the multi-loop approximation with and without mutual inductance between the loops.	30

1 Introduction

Our project addresses the challenges of detecting Unexploded Explosive Ordnances (UXO), which are military explosives such as bombs and grenades that failed to detonate as intended. UXOs are found globally, particularly in regions with histories of prolonged conflict. Contamination remains a serious issue due to limited resources for detection and removal. Each year, an estimated 20,000 people are killed or injured by UXOs UNICEF (2009); Naval Explosive Ordnance Disposal Technology Division (1996), with civilians - especially children - making up around 80% of the casualties. Despite international efforts, UXO clearance remains slow, costly, and technologically demanding.

Conventional detection methods, such as ground-penetrating radar, metal detectors, and explosive-sniffing dogs, have major limitations, including high cost, the need for specialized training, and poor performance at large depths. A major challenge in detecting UXOs in developing countries is distinguishing hazardous UXOs from harmless scrap metal, without the need for expensive tools.

This project was developed under the guidance of Dr. Lindsey Heagy, Assistant Professor in the Department of Earth, Ocean, and Atmospheric Sciences. Dr. Heagys expertise in geophysical inversion and electromagnetic methods was invaluable in shaping our technical approach.

2 Project Overview

2.1 Project Scope

The goal of this project was to design a two-coil electromagnetic survey system capable of identifying buried conductive objects and extracting key properties such as depth, shape, and conductivity. By analyzing the frequency response, we aimed to determine whether it exhibited uniaxial symmetry, which is a trait characteristic of most UXOs and is rarely present in scrap metals.

Key deliverables of the project included:

- A system capable of generating and measuring frequency-domain electromagnetic responses from subsurface conductive objects.
- The ability to acquire reliable, low-frequency data (operating between 1-100 kHz) suitable for near-field sensing applications.
- A signal processing and geophysical inversion pipeline for reconstructing subsurface conductivity distributions from the measured data.
- A framework for classifying detected objects based on their geometric and electromagnetic characteristics, with an emphasis on identifying uniaxial symmetry.

To simulate the response of buried UXOs, we modeled them using a 3-loop approximation, where the object was represented as a single loop or a collection of loops. This simplified the physics while still capturing the essential inductive behavior necessary for simulating eddy currents and secondary field interactions.

The scope of the project was intentionally limited to small-scale field testing and simulated environments, rather than full-scale deployment or real UXO sites. The geophysical inversion algorithm was tested primarily with synthetic data and limited real-world measurements due to time and resource constraints.

2.2 Proposed Solution

Our proposed solution is a two-coil electromagnetic survey tool operating in the frequency domain. The operation of the system is summarized by Fig. 1.

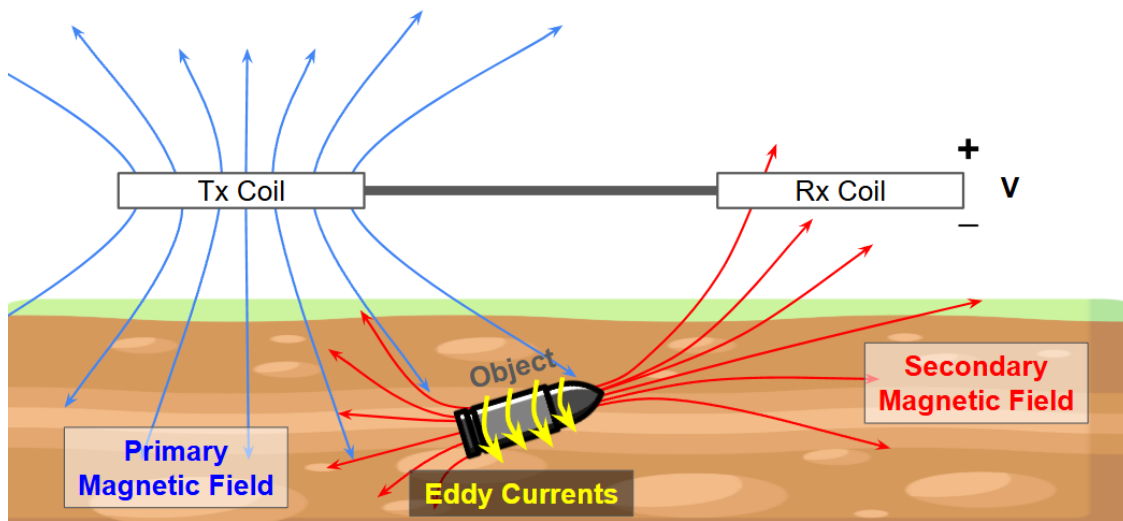


Figure 1: Alternating current is applied to the Tx coil to generate a primary time-varying magnetic field (blue). This field induces eddy currents (yellow) in the buried object. These eddy currents generate a secondary time-varying magnetic field (red), which generates a current and voltage signal in the Rx coil.

To prevent the primary field from interfering with the secondary magnetic field, a bucking coil was added to the system (not shown in Fig. 1). The bucking coil is precisely calibrated to cancel out the direct coupling between the Tx and Rx coils, allowing the Rx coil to more effectively isolate the secondary field generated by the target object.

For simulating this behavior, we used a three-loop approximation, modeling the UXO as one or more conductive loops in the ground. This approach allowed us to compute mutual inductances

and predict the secondary magnetic field generated by the object in response to the primary field.

To extract meaningful information from measured or simulated data, we implemented a geophysical inversion algorithm in Python. This algorithm estimates subsurface properties such as object depth, shape, and relative conductivity.

3 Discussion

3.1 Hardware

The hardware for the system consists of three different coils: the main transmitting (TX) coil and the receiving (RX) coil. There is also a third coil, called a bucking coil, used to cancel out the primary field, so that the only response measured by the receiving coil is from the secondary field. See Fig. 2 for the hardware system-level diagram.

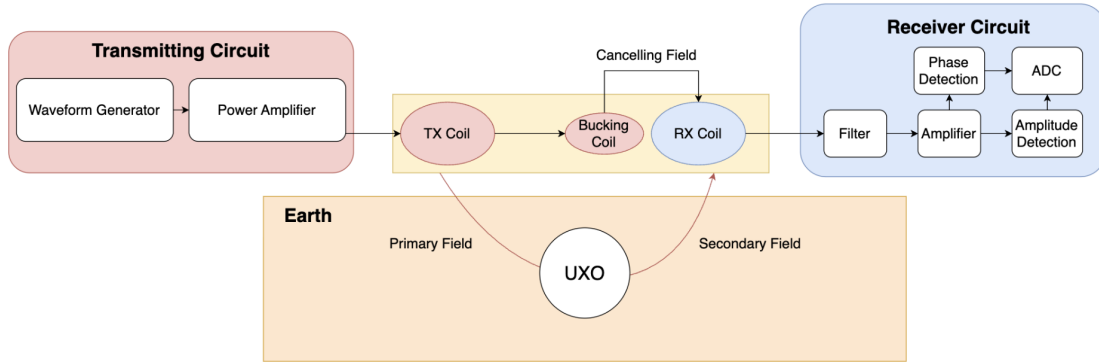


Figure 2: System level diagram for the hardware, including three coils, a receiving circuit, and a transmitting circuit.

The inversion model we are using created several requirements that shaped the design of our system. Our geophysical model uses two approximations in its model: the quasistatic approximation, that the wavelength of our electromagnetic oscillations is significantly larger than the intercoil distance, and the point dipole approximation. These approximations impose the following requirements on our design.

- The intercoil distance should be significantly larger than the coil radius
- The system frequency should stay under 1 MHz
- The intercoil distance should stay on the same order as our depth of investigation.

Detail on the chosen values for the coils and their spacings can be found in tables 2 and 3 in appendix Appendix D.

3.1.1 Transmitting Coil

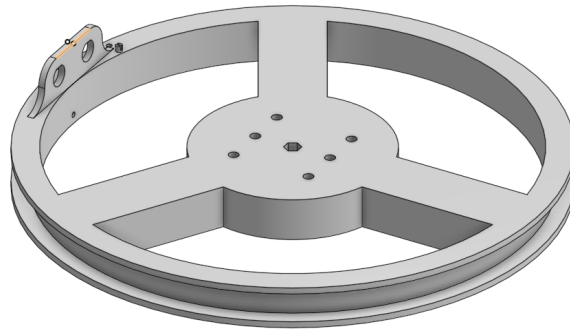


Figure 3: Transmitting coil design

In our design of the transmitting coil system, we wished to optimize for a few different objectives:

- Maximize the gain of the primary magnetic field.
- Have as flat and predictable a frequency response across our desired frequency range.
- Keep the point dipole approximation accurate for our design choices.

Given that the strength of the generated magnetic field scales linearly with the number of turns and with the area of the coil, and that the inductance of the coil scales by the square of the number of turns in the system, we ultimately want to minimize the number of turns and maximize the area of the coil to increase our effective gain. These two optimization parameters are counterbalanced by the minimum specified load of our chosen Tx amplifier, while maintaining the dipole approximation and ease of construction of the coil.

3.1.2 Receiving Coil

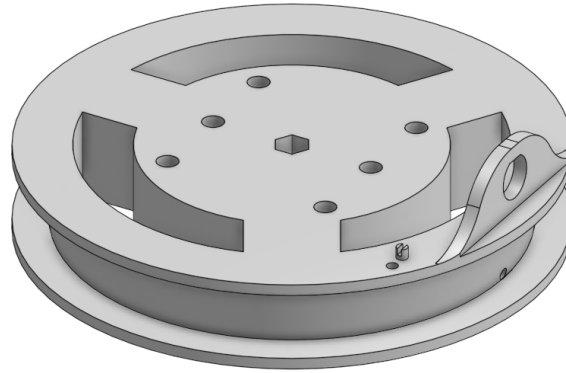


Figure 4: Receiving coil design

The design of the receiving coil was less constrained than the Tx coil, as the gain of the coil scales linearly with the number of turns and coil area. In choosing our parameters, our main concern became keeping the coil small enough that cancellation with the bucking coil was easy to achieve. Another design consideration was keeping the self-resonant frequency of the coil outside our desired frequency range, as it would add significant gain to the system that is difficult to model and would create significant attenuation for high frequencies, as the coil acts as a low-pass filter due to its high inductance. As the self-resonant frequency of the coil results from complex interactions that are hard to model, the number of turns used in the coil was increased, and the resonance was empirically measured until the maximum number of turns for our coil was found.

3.1.3 Bucking Coil

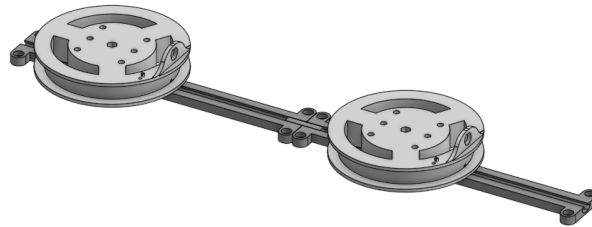


Figure 5: Bucking coil mounting system

The bucking coil was designed to be placed in series with the transmitting coil such that the current through the coil would be perfectly in-phase with the transmitting coil, but wrapped in the opposite direction to create a canceling field. To prevent the bucking coil from creating a significant secondary response, it was designed to be much smaller and closer to the Rx coil than the Tx coil. The winding mount of the coil was a copy of the Rx coil, and only five windings of wire were used. To optimize the inter-coil distance for optimal cancellation, a basic finite element simulation was made in MATLAB to simulate the superposition of the bucking and transmitter coil fields. This model was made by approximating each coil as a two-dimensional circle made up of a series of small current elements, which were then integrated over with the Biot-Savart Law. Then, a range of values was simulated to find the distance with the best cancellation. Implementation information can be found in Appendix E.

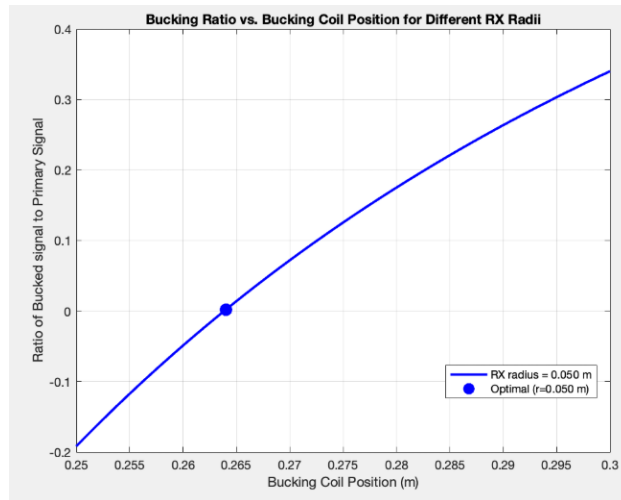


Figure 6: Result of simulating bucking coil cancellation for various distances

3.1.4 Mounting System

To mount the coils and ensure consistent spacing and adjustability, a 3D printed rail system was created to allow adjustable mounting of the coils to a 2x4 used as the backbone for the system. The dimensions of the mounting system were taken from an extruded aluminum mounting rail. A 3D printed system was chosen instead of directly using the extruded aluminum, as we wished to minimize the presence of large metallic objects near the coils to increase the consistency of the system. Images of the full CAD models for the device can be seen in Appendix C

3.1.5 Coil Electrical Model

To find a baseline value of the primary magnetic field seen at the receiving coil with no secondary coupling to the environment, an accurate model of the transfer function between the coils must

be constructed. The TX coil was modeled as a simple inductor in series with a resistor, using its measured inductance value. The RX coil had a more complex transfer function due to its high number of windings, resulting in a large self-capacitance, but for our purposes, it was modeled as a self-resonant low pass filter where with a transfer function that could be curve fit to a model using measurements and MATLAB. The interaction between the two coils can be modeled using a mutual inductance, which models the magnetic coupling between the coils. This gives a final transfer function between the coils as follows:

$$\frac{V_{rx}}{V_{tx}} = tf_{rx}(\omega) \frac{-\mu_0 \omega i}{4\pi r^3} \frac{1}{R_{tx} + L_{tx}\omega} \quad (1)$$

Where $tf_{rx}(\omega)$ is a measured transfer function of the Rx coil found by curve fitting the voltage response of the coil.

3.2 Circuitry

3.2.1 Transmitting Circuit

The transmitting circuit needs to be able to drive the transmitting coil to establish a sufficiently strong magnetic field to detect underground objects. The requirements for this circuit is that it needs to be able to: (a) drive a highly inductive load, (b) drive a low resistive load, and (c) operate at 1 to 100kHz. The requirements of the system are conveniently all satisfied by an audio amplifier, which achieves all three. Thus, an off-the-shelf audio amplifier is an ideal solution. Our team selected the LM1875 amplifier from Texas Instruments.

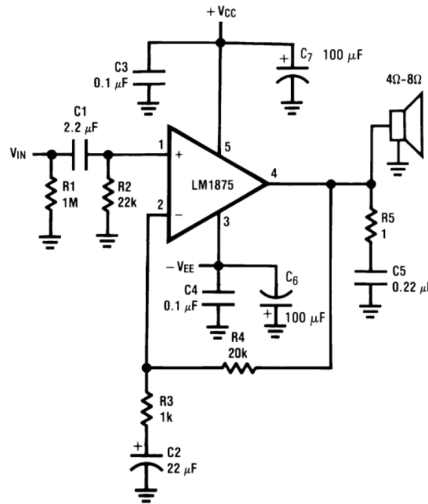


Figure 7: LM1875 Audio Amplifier [Texas Instruments (2004)].

3.2.2 Receiving Circuit

The objective of the receiver circuit is to measure the response of the system (magnitude and phase) and provide this information to a microcontroller. Figure 8 showcases a system-level diagram showing the receiving circuit.

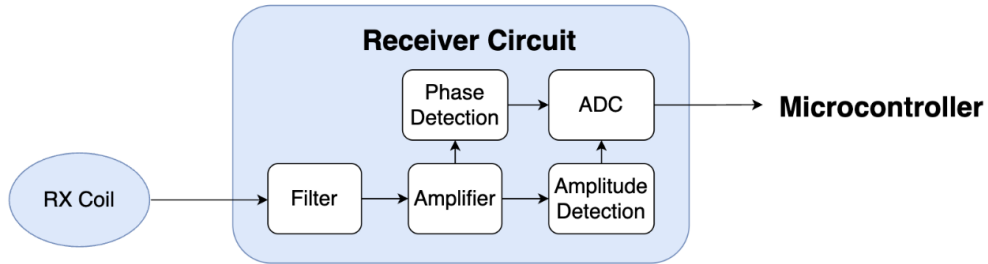


Figure 8: System-level diagram of receiver circuit. The signal from the Rx coil is filtered and amplified. Then this processed signal goes through amplitude and phase detection stages to measure the response.

The filter and amplifier is implemented by constructing two biquad filters in series, which are both second-order filters. See Appendix A for the schematic. Strong filtering was required due to the weak signal strength received on the Rx coil. The center frequency is 20kHz, and the filter can successfully filter and amplify (Fig. 9).

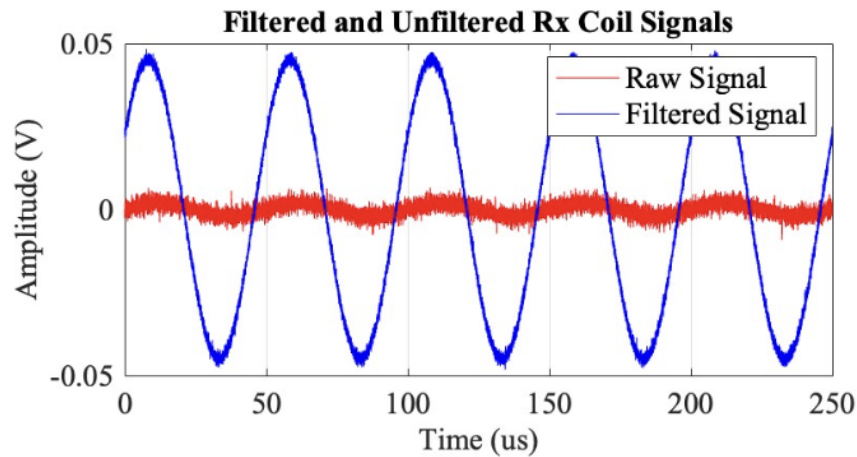


Figure 9: The filtered and raw Rx signals.

Notably, since the Rx circuit must perform analog phase detection, the response functions for the circuits must be measured using a network analyzer to compensate for any phase shifts introduced by the circuits. The phase response is plotted in Appendix A.

After being filtered and amplified, the Rx signal passes through two parallel stages: (1) analog phase detection and (2) amplitude detection to measure the full response of the system.

1. Analog Phase Detection:

The analog phase detection circuit outputs a DC voltage which is proportional to the phase difference between the Tx and Rx signals (Fig. 10). Several stages are used to achieve this transformation.

- (a) The Tx and Rx signals in are typically significantly different in amplitude (Signal (A), Fig. 10).
- (b) Two comparators are used to transform the two sinusoidal signals into two offset square waves of identical amplitude (Signal (B), Fig. 10).
- (c) Then, an exclusive OR (XOR) gate is used to transform the comparator signals into short pulses with time-width proportional to the phase offset between the Rx and Tx signals. (Signal (C), Fig. 10).
- (d) Finally, the short pulses are passed through an RC filter to produce a DC signal proportional to the phase difference (Signal (D), Fig. 10).

This sophisticated circuit design allows the phase information between the two coils to be fully captured through one measurement on a microcontroller, significantly reducing the firmware requirements of the project.

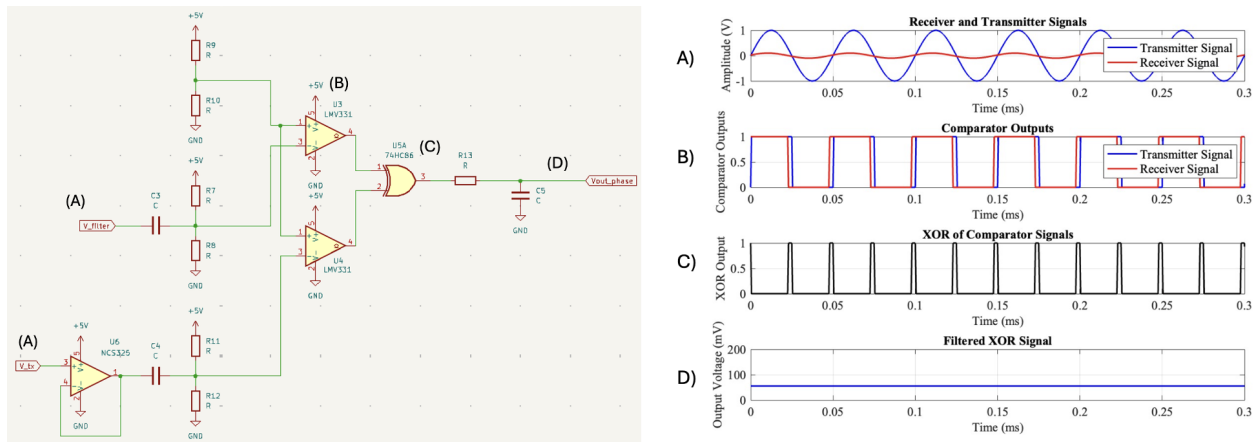


Figure 10: Analog phase detection circuit.

2. Amplitude Detection Circuit:

Amplitude detection is required to measure the magnitude of the signal on the receiving coil. Magnitude detection can be achieved through a simple half or full-wave rectifier. For the

purpose of this project, a half-wave rectifier is the better option because it requires fewer components, and a large output signal is not required, as the signal is simply measured and does not drive a load.

3.3 Firmware

The hardware needs to be fully integrated through firmware to collect raw data from a microcontroller and then transmit this data onto a laptop to conduct geophysical inversion. The microcontroller collects magnitude and phase data from the receiver circuit, and acceleration data from an inertial measurement unit (IMU) to determine position. The controller then transmits this data onto a laptop in real time using the communication protocol UART. See figure Fig. 11 for a firmware system diagram.

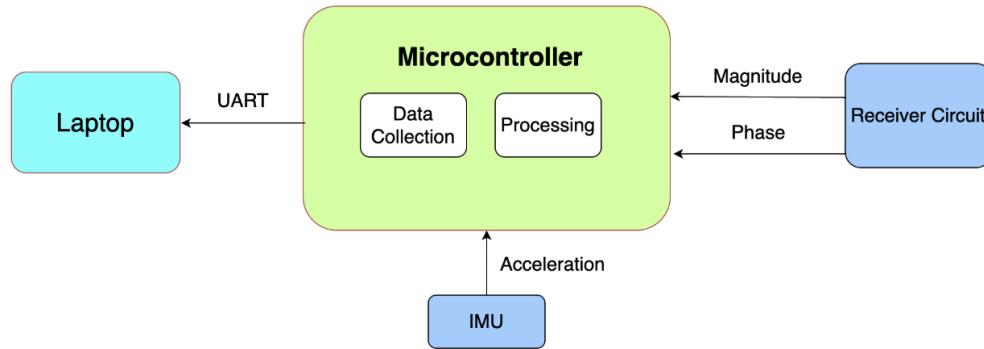


Figure 11: System-level diagram for the firmware.

For this project, the microcontroller used was the STM32L476RG on a Nucleo board. See Appendix B for information on microcontroller selection. Position data was collected using an IMU, future investigations should consider combining this data with a GPS to get more accurate and stable measurements.

3.4 Dataset Acquisition

3.4.1 Motivation

With our hardware and electrical system able to collect data, the next step is to be able to analyze the data and make inferences. One of the primary goals of this project, outlined in Section 2.1, was to create a geophysical inversion pipeline capable of reconstructing subsurface conductivity distributions from measured data. Training and evaluating an inversion model to perform this task requires a significant amount of labeled data.

A simple solution would be to find and use an existing dataset. While this may work for many data inference tasks, this was not feasible for our project. The expected responses are highly dependent on the geometry of the sensor. Design choices such as the distance between the coils, the effective area of the coils, and even the coil inclination angle or number of receiver coils are different across existing sensors. Any data collected by a sensor that does not have the same physical parameters will give different responses, meaning a model trained with the data collected from these sensors would be incompatible with the data collected from the sensor we developed.

Creating a dataset with data measured from the sensor we developed would work well, but it presented some logistical issues. It would require our team to fully complete our physical system before any data could be collected. Given the eight-month timeline of this project, this was not ideal. The data collection process would also likely be time-consuming, requiring us to bury objects with well-characterized shapes and conductivities at measured depths, angles, and locations.

Our team ultimately decided to generate our training dataset using a numerical physics-based approximation of the response, tailored to our system. This approach offers several advantages:

- This allows us to generate a large number of samples with a wide variety of parameters quickly.
- We can create the dataset before the physical system is fully completed, allowing us to parallelize our workflow.
- The ground-truth data describing the shape, conductivity, and location of the objects are defined in the simulation and do not have to be measured.
- The forward simulation was used to simulate different physical parameters for our system, such as the inter-coil spacing and the operation frequency range, which helped us determine ideal system parameters to use in our physical design.

3.4.2 Three-Loop Approximation

There are many ways to perform a forward simulation. One approach is to use finite element analysis (FEM) with Maxwell's equations to describe how the magnetic fields behave in the buried object. While this approach would give the most accurate results, it can be very computationally demanding. For objects with a symmetry, a physics-based approximation can yield results with similar accuracy to FEM. For the application of identifying UXOs, they are typically uniaxial with shapes similar to a spheroid or cylinder Simms et al. (2004); Naval Explosive Ordnance Disposal Technology Division (1996). Due to this cylindrical symmetry, the secondary magnetic field will typically exhibit a dipole response Breiner (1999). Fig. 12 shows an example of what real UXOs can look like, along with their measured response using a similar system to the one we constructed.

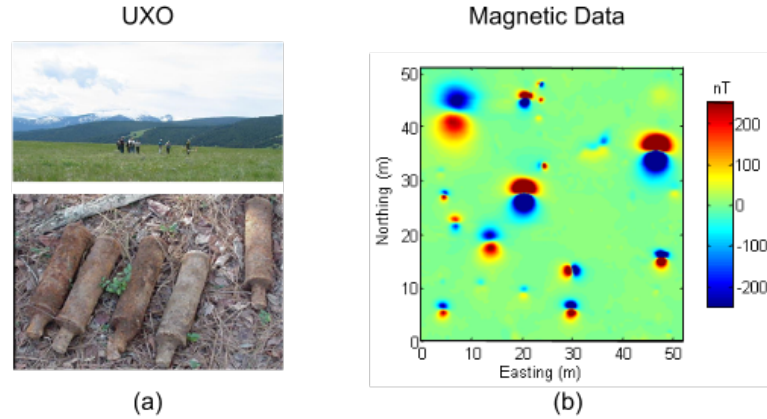


Figure 12: Image from Oldenburg et al. (2017) of a real UXO used in a field survey (a). Magnetic data from a field survey with buried UXOs from (a) using a two-coil system (b). The measured response is similar to what one might see from a perfect dipole.

Due to the strong similarity between a UXO and a perfect dipole, a reasonable approximation of the magnetic response can be achieved by replacing the UXO with a loop with some internal inductance and resistance shown in Fig. 13. This was simulated in Python with an example output shown in Fig. 14. This model also allows us to ignore the conductivity of the ground because it will be negligible in comparison to that of the object or loop. A full derivation of the algorithm used is outlined in Appendix F.1.

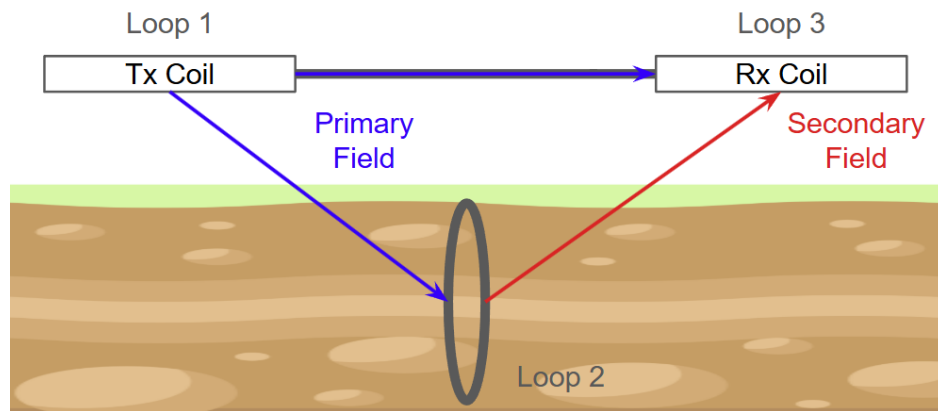


Figure 13: Diagram of the three-loop approximation model. The Tx coil (loop 1) induces a primary magnetic field (blue), which is felt by the object represented as a wire loop (loop 2) and the Rx coil (loop 3). The object induces a secondary magnetic field (red) also felt at the Rx coil.

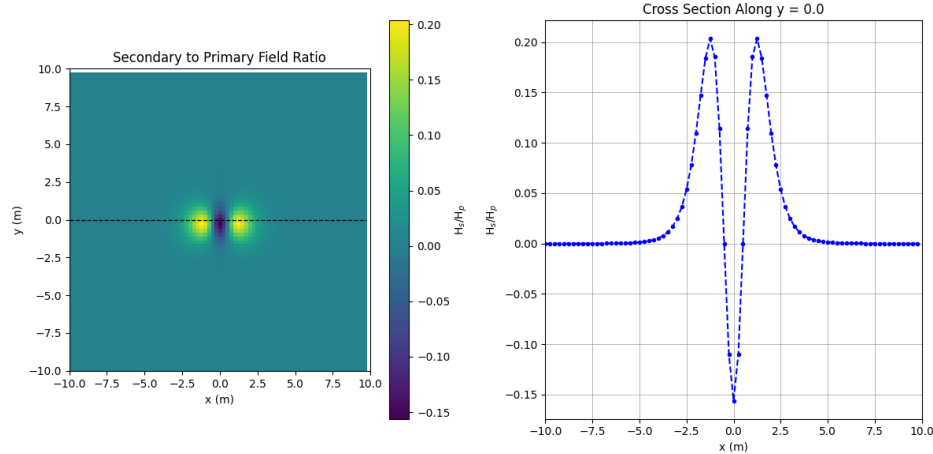


Figure 14: Example of the primary-to-secondary field ratio using the three-loop approximation. A 2D heat map is shown on the left, with a 1D slice along the line $y = 0$ shown on the right.

3.4.3 Multi-Loop Approximation

The three-loop approximation does a good job of displaying the dipole characteristics of the UXO response; however, in performing this approximation, information about the shape and conductivity of the object is lost. This information is required to successfully reconstruct a conductivity mapping of the object from the magnetic data. To get around this issue, we represented the object as a superposition of loops evenly spaced along the length of the object demonstrated in Fig. 15.

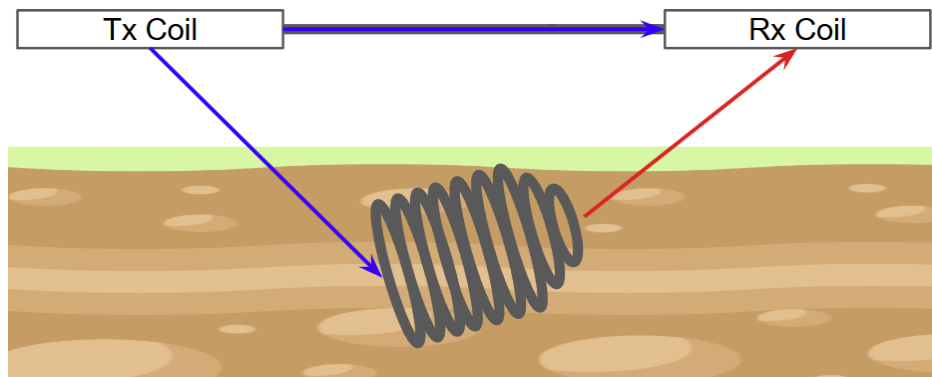


Figure 15: Diagram of the multi-loop approximation model. The UXO object is represented as a collection of linearly spaced loops centered along its axis of symmetry. The Tx coil emits a primary magnetic field (blue), which is felt by the object and the Rx coil. The object emits a secondary magnetic field (red).

The span of the loops, along with their radii, encodes the shape of the object. The conductivity and permeability of the object are encoded in the resistance and inductance values of the loops.

The output in Fig. 16, demonstrating a realistic scenario of a 30° inclination angle, is similar to the field measurements in Fig. 12, indicating the approximation gives the expected result. Using this forward simulation model, random uniform distributions for parameters such as the angle, depth, conductivity, and shape of the UXO were used to generate a dataset to train our geophysical inversion model. A derivation of this model is outlined in Appendix F.2.

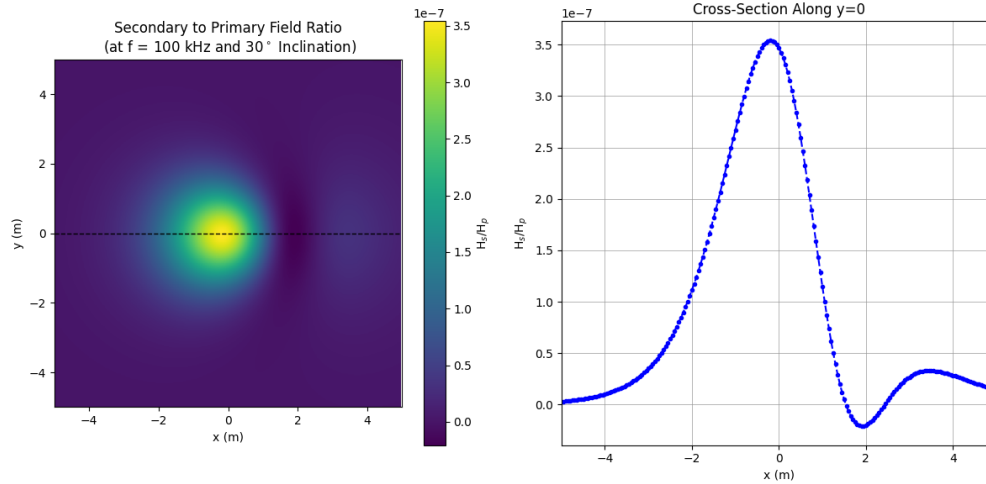


Figure 16: Example of the primary-to-secondary field ratio using the multi-loop approximation. A 2D heat map is shown on the left, with a 1D slice along the line $y = 0$ shown on the right.

3.5 Geophysical Inversion

Geophysical inversion is a technique used to infer the physical properties of the subsurface from measured geophysical data. In the context of this project, inversion plays a critical role in transforming electromagnetic measurements into meaningful models of the underground environment. Specifically, it enables the estimation of the size, shape, and depth of buried objects, which is essential for distinguishing between UXO and scrap metal.

3.5.1 Inversion Algorithm Overview

For this project, we developed a Python-based inversion algorithm. The implementation was guided by methodologies presented in Deidda et al. (2019) and Buccini and Daz de Alba (2021), both of which describe advanced electromagnetic inversion frameworks. Our approach uses the nonlinear forward modeling approach described in Deidda et al. (2019), which provides accurate simulation of electromagnetic responses for complex subsurface structures.

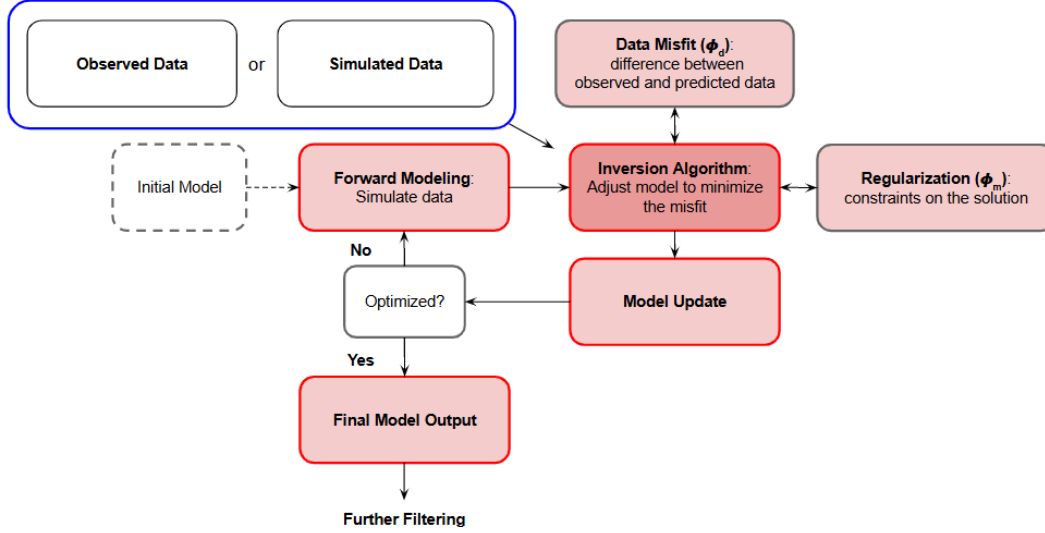


Figure 17: Iterative Inversion Workflow

Fig. 17 illustrates the iterative process of solving an inverse problem using geophysical data. Starting from an initial model, forward modeling is used to simulate predicted responses, which are compared against measured or synthetic data. The inversion algorithm then updates the model to minimize the objective function:

$$\phi = \phi_d + \lambda \phi_m \quad (2)$$

where ϕ_d is the data misfit, ϕ_m is a regularization term and λ is the trade-off parameter. The inversion loop continues until a convergence criterion is met. Detailed mathematical explanation for each step are provided in Appendix G.

The inversion can be run on synthetic data generated using the multi-loop model described in Section 3.4.3, the forward model used within the inversion algorithm, or real measurements collected using our instrument.

Due to computational constraints, each iteration takes approximately 40-60 seconds, making it impractical to fully optimize the model. We found that after roughly 30 iterations, further updates primarily affect the magnitude of the recovered conductivity, with minimal change in geometry. Since UXOs are known to exhibit high conductivity, recovering relative contrast is more important than the actual conductivity values for our application.

Hence, we implemented a post-inversion filtering step that retains only regions with conductivity exceeding 60% of the maximum value. This enhances the visibility of highly conductive targets under the assumption that UXOs produce the strongest EM responses. Even if a strong response originates from a non-UXO object, it can often be distinguished based on its lack of uniaxial symmetry. Therefore, this filtering approach is both effective and appropriate for UXO detection.

3.5.2 Inversion Test Result

To validate the inversion algorithm, we performed a simulation using a synthetic conductivity model containing a high-conductivity cylindrical target, representing a UXO. The left panel of Fig. 18 shows the 2D cross-section of this model, discretized into horizontal soundings and depth layers. The right panel displays the corresponding simulated electromagnetic response across a range of frequencies, computed using the same forward model employed in the inversion process. This simulated dataset serves as the input to the inversion algorithm.

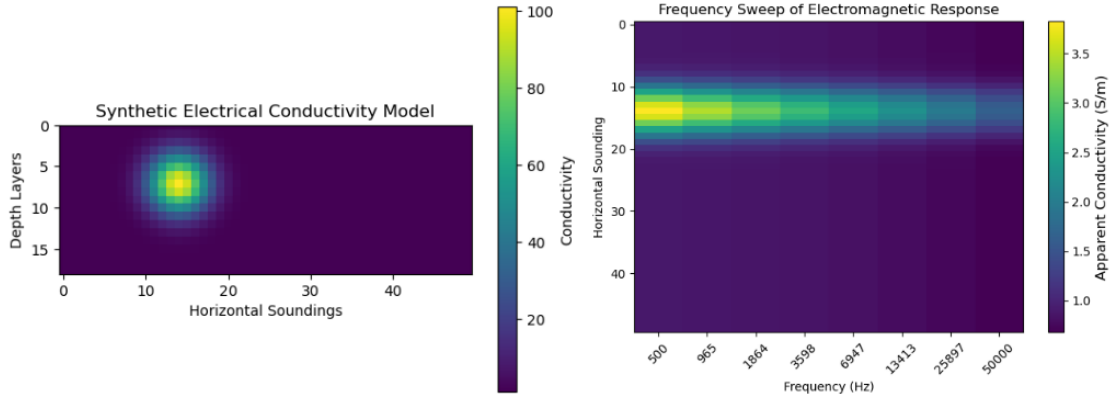


Figure 18: Synthetic conductivity model with a cylindrical target (left) and Simulated data across multiple frequencies and positions (right)

Fig. 19 shows the results after running the inversion algorithm. The left panel shows the reconstructed conductivity distribution after inversion and post-inversion filtering. The target is recovered as a slightly vertically elongated circular anomaly, with good spatial agreement in both depth and horizontal position compared to the true model. The recovered radius also closely matches that of the original target. A few minor artifacts appear near the surface, likely due to noise or instability in early iterations. The right panel shows the electromagnetic response predicted by the recovered model, which closely resembles the original simulated data, capturing the key frequency-dependent trends and spatial localization of the anomaly.

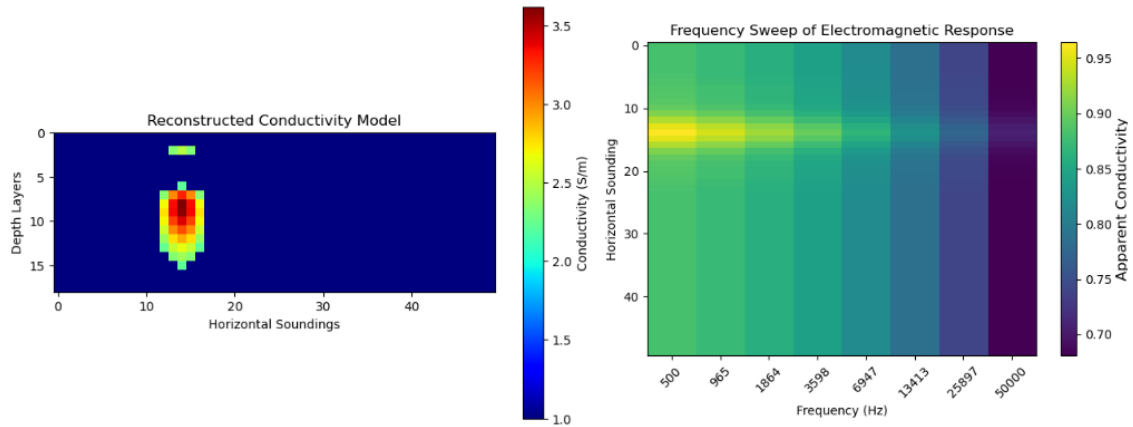


Figure 19: Reconstructed conductivity model after inversion and filtering (left) and Simulated data from the reconstructed model (right)

The magnitude of the recovered conductivities and their electromagnetic response are attenuated, which is a known effect of regularization and early stopping. Despite this, the geometry and high contrast of the anomaly compared to its surroundings are well-preserved, which is the most critical information for UXO detection applications. Therefore, this test overall confirms that the inversion algorithm can reliably recover the location and shape of buried conductive targets, even under practical constraints such as limited iterations and simplified regularization.

Although the inversion algorithm has not yet been tested with controlled buried conductive objects, preliminary tests using real data collected on campus have been promising. A sweep across a grassy area produced a subsurface conductivity map showing layered structures with varying thickness, as shown in Fig. 20. This is consistent with expectations for natural stratification of soil and rock.

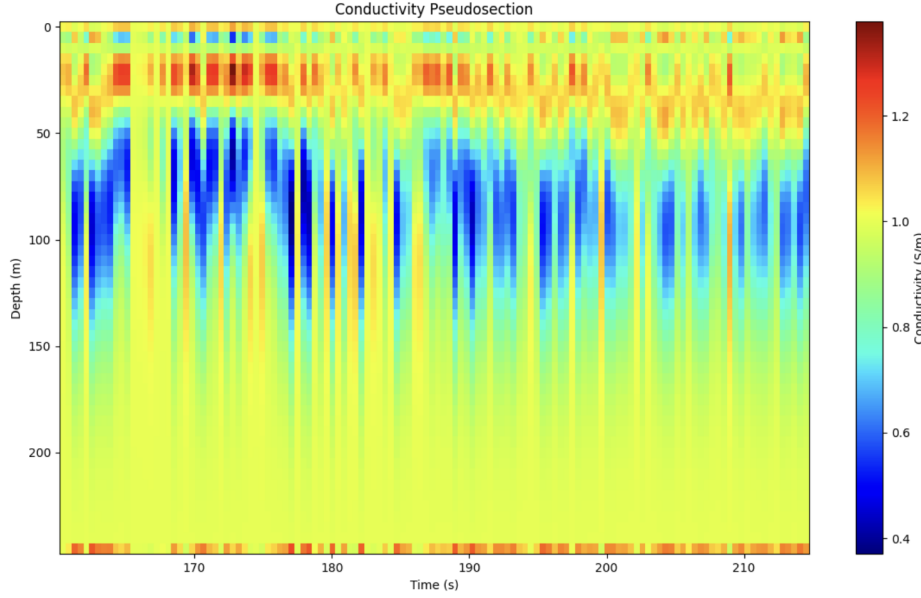


Figure 20: Inversion result over a strip of grass

These results suggest that the inversion process is functioning correctly and is capable of producing meaningful results when deployed in real UXO detection scenarios.

4 Conclusions

The goal of our capstone was to develop an electromagnetic system capable of imaging underground regions to detect UXOs. Through our one-year project, our team successfully built a hardware prototype of a two-coil system used for subsurface imaging and also designed a physics-informed software pipeline to invert raw electromagnetic data into an underground map.

The proposed two-coil system was able to measure the electromagnetic response of underground regions. A transmitting coil establishes a time-varying magnetic field, which induces underground eddy currents, leading to a secondary magnetic field, which induces a voltage measured on the secondary coil. The hardware of the system was able to measure both the phase and magnitude of the secondary field, while canceling the primary field through the use of a third bucking coil.

Our hardware was able to interface with our software pipeline and use geophysical inversion to recreate a crude map of an underground region. The inversion method used an iterative approach to derive a final image that had features that resembled the actual data. By reconstructing the shape of underground regions, we can classify underground objects as uniaxial, providing a solution to mitigate the global UXO problem.

5 Recommendations

Our team has 4 primary recommendations for future investigation:

1. Investigate and implement machine learning models for geophysical inversion and UXO classification. This can include running a small classification network to identify UXOs in real time, or a more complex model to allow efficient full 3D inversion.
2. Go beyond the traditional two-coil system to allow for measurements with higher dimensionality, leading to more accurate inversion. This could include varying more parameters than just frequency, such as coil orientation or number of coils, and creating more advanced inversion pipelines to handle the data that comes from these devices.
3. Fully integrate together the receiving circuits into the surveying device such that the surveyor can act as a standalone unit without needing a laptop attached to provide more flexibility and ease of use in the field.
4. To improve the inversion algorithm, we recommend implementing tools for better parameter tuning. Conducting an L-curve analysis can help identify the optimal trade-off parameter, λ . Additionally, exploring spatially adaptive regularization, where λ varies with depth or known geological features, could enhance resolution in target zones.

6 Deliverables

1. Physical Two-Coil System
2. Circuit Schematics
3. Circuits
4. Cad Models
5. Github Repo

A Circuit Schematics

A.1 Filter and Amplifier

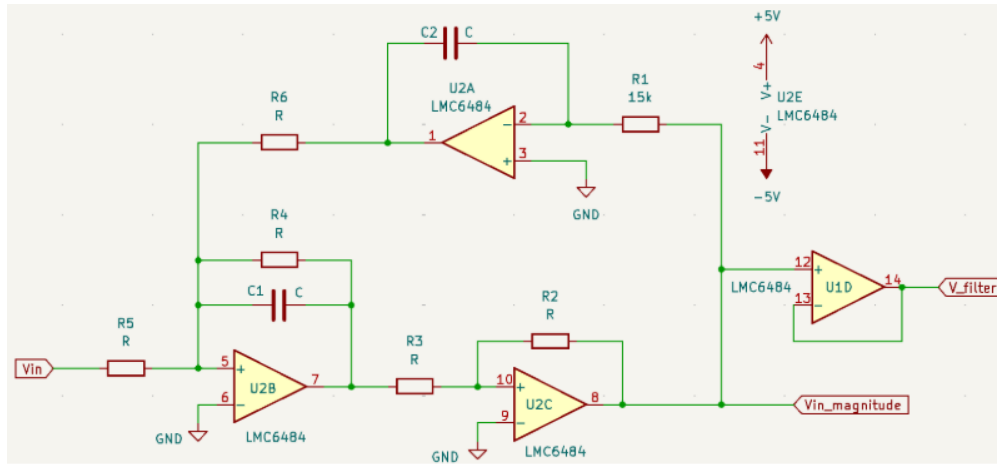


Figure 21: Schematic of a biquad filter.

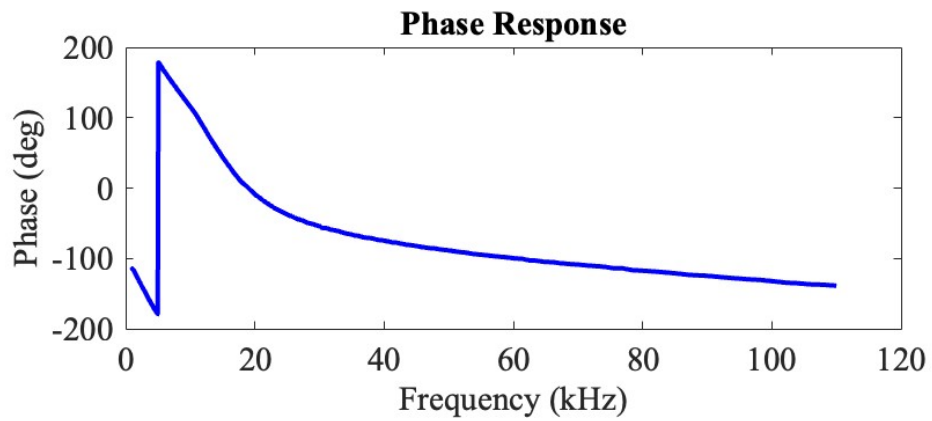


Figure 22: Phase response of two biquad filters in series.

A.2 Analog Phase Detection

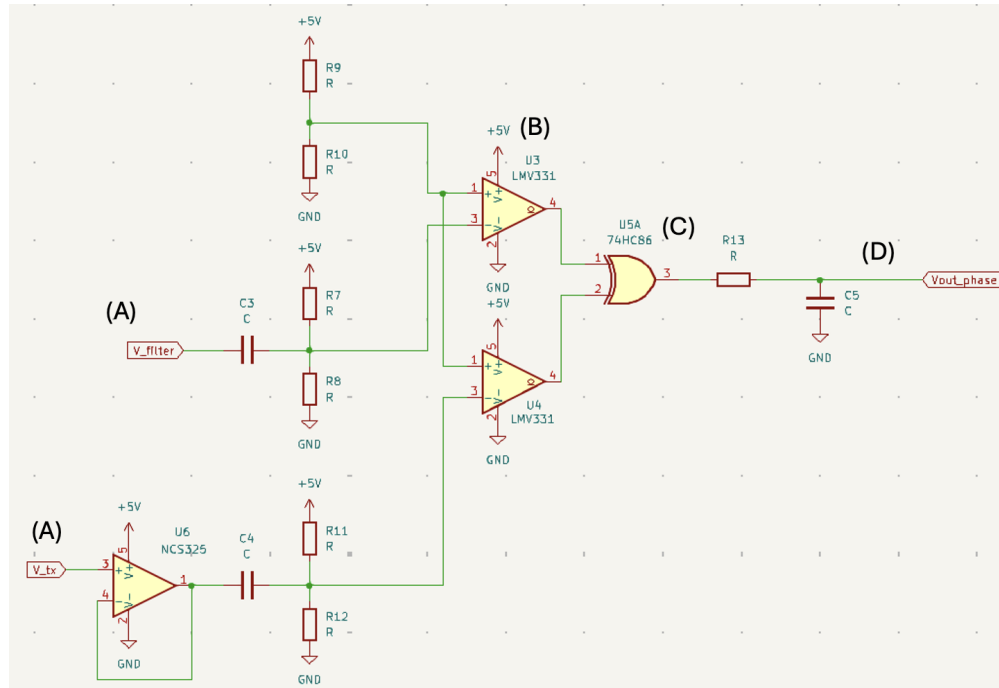


Figure 23: Schematic of analog phase detection circuit.

A.3 Amplitude Detection

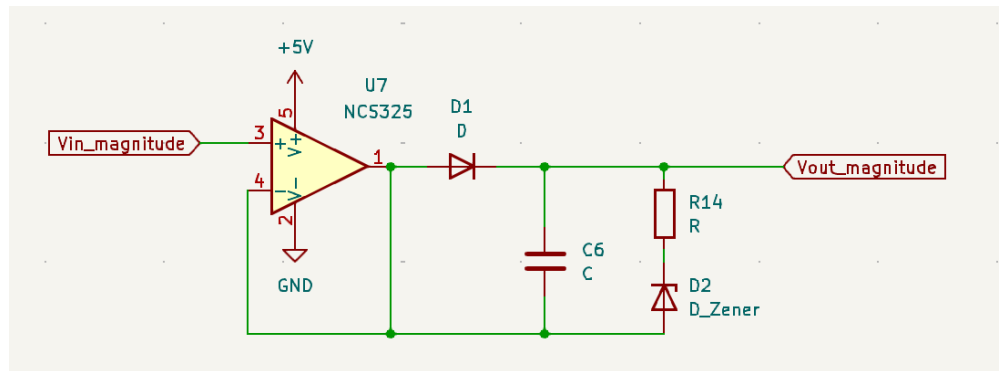


Figure 24: Schematic of amplitude detection circuit.

B Microcontroller Selection

Initially, the microcontroller that was used was the STM32F103C8T6 Bluepill controller due to familiarity. However, after facing hardware limitations, this was changed to a STM32L476RG con-

troller on a Nucleo Board. The table below showcases a comparison of these two microcontrollers, showcasing the most significant differences for our project.

Feature	Bluepill	Nucleo Board
Microcontroller	STM32F103C8T6	STM32L476RG
ADC	1 Msps	5 Msps, oversampling
Flash Memory	128KB	1MB
RAM	20KB	128KB
On-board debugger	N/A	ST-LINK

Table 1: Comparison between the Bluepill and Nucleo Board microcontrollers.

C CAD of Coil Winding Holders

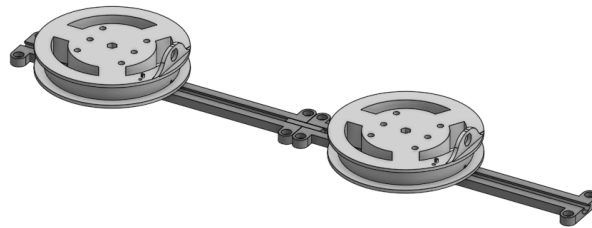


Figure 25: Bucking coil mounting arrangement

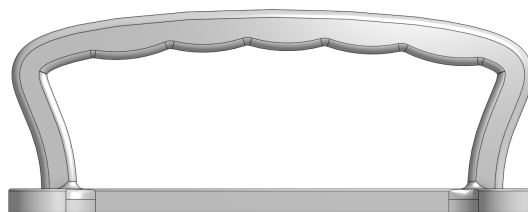


Figure 26: Carrying Handle

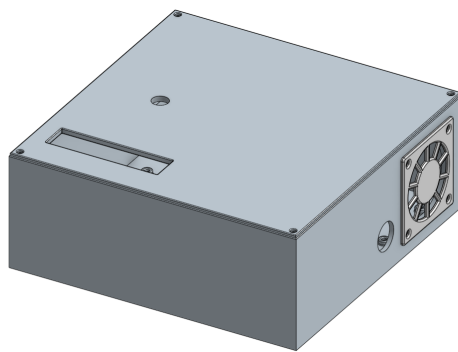


Figure 27: Electronics Box

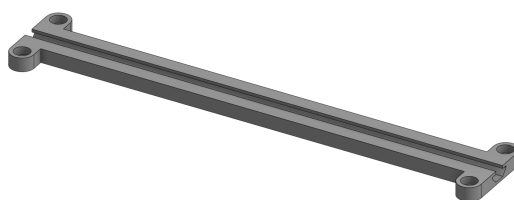


Figure 28: Mounting Rail

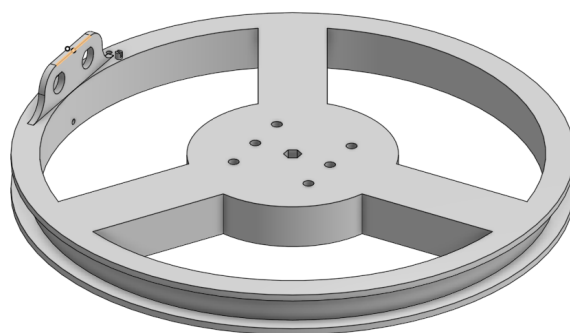


Figure 29: Transmitting Coil

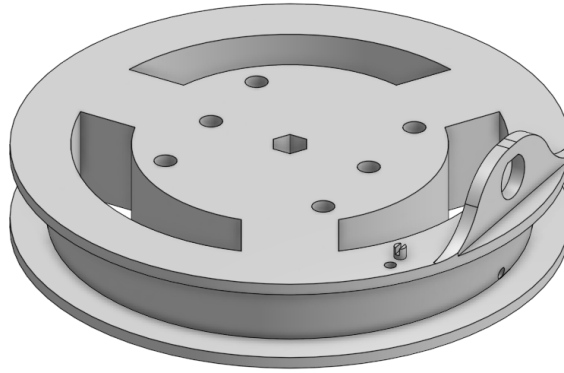


Figure 30: Receiving Coil

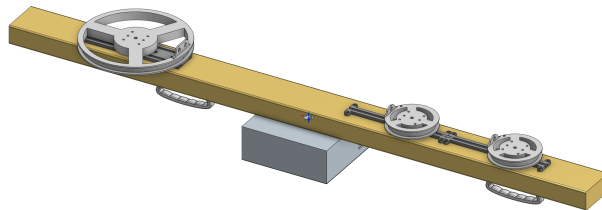


Figure 31: Full Assembly

The complete CAD models and assembly can be found [here](#).

D Physical Coil Parameters

The construction parameters of the TX, RX, and Bucking coils are as follows.

Parameter	RX Coil	TX Coil	Bucking Coil
Number of turns	250	5	40
Radius	5cm	5cm	11.5cm
Wire Gauge	32	26	26
Resistance	41.7Ω	N/A	4.0Ω
Inductance	$11.3mH$	N/A	$0.89mH$

Table 2: Table of values for each coil parameter

For our purposes, the resistance and inductance of the bucking coil were considered negligible compared to the contributions of the TX coil, such that placing the bucking coil in series with the TX coil would have negligible effect on the impedance of the total system.

The overall construction parameters of the physical system are as follows, the values in 'used' mark the values we used in our final system demonstration:

Value	Min.	Used	Max
TX-RX distance	0.65m	0.9m	1.1m
Bucking-RX distance	15 cm	26.05cm	30cm
Frequency	300 Hz	N/A	100kHz

Table 3: The range of physical parameters possible for our 3 coil system and the chosen values for our demonstration system.

Since the system was designed with flexibility in mind with an adjustable rail system to mount the coils, a range of values is available for the inter-coil distance.

E Bucking Simulation

To simulate the bucking coil system, the magnetic field created by the combination of TX and bucking field was approximated using the Biot-Savart Law:

$$B = \int \frac{\mu_0 I \hat{r} \times ds}{4\pi r^2} \quad (3)$$

where ds represents a single infinitesimal current element. The rx coil area was then discretized into a $n \times m$ grid, and the bucking coil and TX coil were both broken up into current elements and summed up for each element $B_{i,j}$ at grid location (x_i, y_i) . The final magnetic field at each point was then calculated as

$$B_{i,j} = \sum_k \frac{\mu_0}{4\pi} \frac{N_k \vec{J}_k \times \vec{r}_{ijk}}{r_{ijk}^3} \quad (4)$$

Where N_k is the number of turns in the coil section \vec{J}_k is the current vector for the coil section, and \vec{r}_{ijk} represents the distance vector between the simulation cell and the current vector.

F Forward Simulation Algorithms

F.1 Three-Loop Approximation Model

Following the behavior described by Fig. 13, this model aims to measure the primary-to-secondary field ratio using the method outlined by GeoSci Developers (2018).

Our system operates by supplying an alternating current (AC) with angular frequency ω to the Tx coil, which can be represented by Eq. (5).

$$i_1(t) = I_1 e^{j\omega t} \quad (5)$$

The derivative form of Faraday's law gives Eq. (6).

$$\mathcal{E} = -\frac{\partial \Phi_B}{\partial t} \quad (6)$$

The mutual inductance between two loops is given by Eq. (7), which can be rearranged to give Eq. (9).

$$M_{ij} = \frac{\Phi_{ij}}{i_i} \quad (7)$$

$$M_{ij} i_i = \Phi_{ij} \quad (8)$$

$$M_{ij} \frac{\partial i_i}{\partial t} = \frac{\partial \Phi_{ij}}{\partial t} \quad (9)$$

Combining Eq. (6) and Eq. (9) gives Eq. (10), which relates the current from one loop to the EMF induced by another loop.

$$\mathcal{E}_j = -M_{ij} \frac{di_i}{dt} \quad (10)$$

This means that when we supply a time-varying current to the transmitting coil, it will induce an EMF in the object coil and the receiving coil proportional to the mutual inductances between the coils. This is shown in Fig. 32.

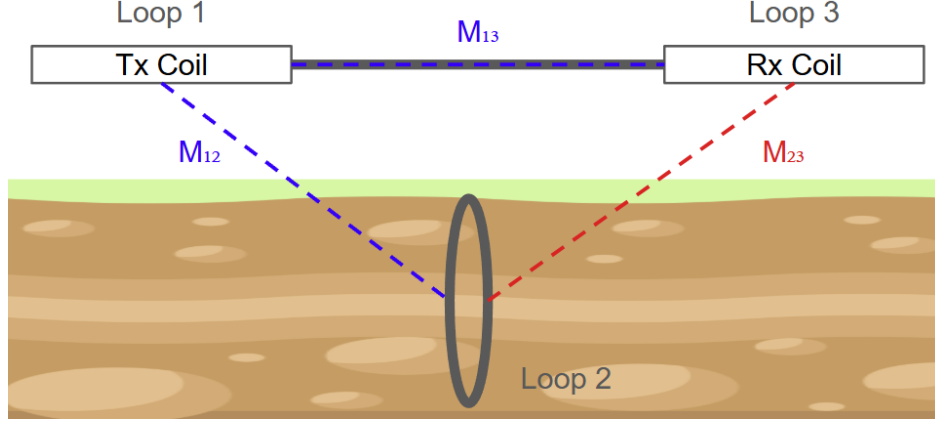


Figure 32: Mutual induction between loops in the three-loop approximation.

The mutual inductance from Eq. (8) can be expressed as an integral over the magnetic field in Eq. (11).

$$M_{ij}i_i = \iint \mathbf{B}_i \cdot d\mathbf{a}_j \quad (11)$$

The magnetic field can be expressed as the vector potential in Eq. (12).

$$\mathbf{B} = \nabla \times \mathbf{A} \quad (12)$$

Using Stokes' Theorem with Eqs. (11) and (12) gives Eq. (13).

$$M_{ij}i_i = \iint (\nabla \times \mathbf{A}_i) \cdot d\mathbf{a}_j = \oint \mathbf{A}_i \cdot d\mathbf{l}_j \quad (13)$$

Applying the Biot-Savart law from Eq. (14) to Eq. (13) yields Eq. (15).

$$\mathbf{A} = \frac{\mu_0 I}{4\pi} \oint \frac{d\mathbf{l}}{|\mathbf{r} - \mathbf{r}'|^2} \quad (14)$$

$$M_{ij}i_i = \frac{\mu_0 i_i}{4\pi} \oint \left(\oint \frac{d\mathbf{l}_i}{|\mathbf{r} - \mathbf{r}'|^2} \right) \cdot d\mathbf{l}_j \quad (15)$$

This simplifies to express mutual inductance in Eq. (16) that only depends on the geometry of the loops and their relative positions.

$$M_{ij} = \frac{\mu_0}{4\pi} \oint \left(\oint \frac{d\mathbf{l}_i}{|\mathbf{r} - \mathbf{r}'|^2} \right) \cdot d\mathbf{l}_j \quad (16)$$

Using the primary current from Eq. (5), Eq. (10), and the result from Eq. (16), we can fully characterize the EMFs induced by the primary magnetic field on loops 2 and 3 from Fig. 32 as Eqs. (17)

and (18) respectively.

$$\mathcal{E}_2^p = -j\omega M_{12} I_1 e^{j\omega t} \quad (17)$$

$$\mathcal{E}_3^p = -j\omega M_{13} I_1 e^{j\omega t} \quad (18)$$

The EMF of loop 3 induced by the secondary field in Eq. (19) requires us to know the current in loop 2.

$$\mathcal{E}_3^s = -M_{23} \frac{di_2(t)}{dt} \quad (19)$$

We can utilize Kirchhoff's voltage law to find this current, which states that the closed-loop sum of voltages must be zero. In the case of a wire loop, the driving voltage will be opposed by the resistance in the wire along with the reactance related to the self-inductance of the loop. This will generate an opposing EMF described by Eq. (20).

$$\mathcal{E}^\dagger = i(R + j\omega L) \quad (20)$$

Eqs. (17) and (20) allow us to solve for the current i_2 in Eq. (23)

$$\mathcal{E}_2^p + \mathcal{E}_2^\dagger = 0 \quad (21)$$

$$-j\omega M_{12} I_1 e^{j\omega t} + i_2(R + j\omega L) = 0 \quad (22)$$

$$i_2 = \frac{j\omega M_{12} I_1 e^{j\omega t}}{R + j\omega L} \quad (23)$$

Plugging this into Eq. (19) gives a secondary EMF felt at the Rx coil described by Eq. (24).

$$\mathcal{E}_3^s = \frac{\omega^2 M_{12} M_{23} I_1 e^{j\omega t}}{R + j\omega L} \quad (24)$$

From Faraday's law, we know the strength of the magnetic field is proportional to the EMF. This allows us to express the ratio of the primary and secondary field strengths as the ratio of the EMFs, giving the frequency-dependent response in Eq. (25).

$$\frac{H^s}{H^p} = \frac{\mathcal{E}_3^s}{\mathcal{E}_3^p} = \frac{M_{12} M_{23}}{M_{13} L} \left(\frac{j\omega L / R}{1 + j\omega L / R} \right) = \frac{M_{12} M_{23}}{M_{13} L} \frac{\alpha^2 + j\alpha}{1 + \alpha^2}, \quad \alpha = \frac{\omega L}{R} \quad (25)$$

The mutual inductances are dependent on the position of the sensor relative to the object (loop 2). This expresses the response of the object as a function of the xy-position and the driving frequency of the sensor.

F.2 Multi-Loop Approximation

This approach can be generalized to contain N loops to form the multi-loop approximation model. If we denote the transmitting loop as T and the receiving loop as R , the EMF for each loop k can be expressed by Eqs. (26) and (27).

$$\mathcal{E}_k^p + \mathcal{E}_k^\dagger + \sum_{k \neq l} \mathcal{E}_k^l = 0 \quad (26)$$

$$\left(-j\omega M_{Tk} I_T + (R_k + j\omega L_k) I_k - j\omega \sum_{k \neq l} M_{kl} I_l \right) e^{j\omega t} = 0 \quad (27)$$

Eq. (26) can be used to form the linear system represented in Eq. (28).

$$\begin{bmatrix} R_1 + j\omega L_1 & -j\omega M_{12} & \cdots & -j\omega M_{1N} \\ -j\omega M_{21} & R_2 + j\omega L_2 & \cdots & -j\omega M_{2N} \\ \vdots & \vdots & \ddots & \vdots \\ -j\omega M_{N1} & -j\omega M_{N2} & \cdots & R_N + j\omega L_N \end{bmatrix} \begin{bmatrix} I_1 \\ I_2 \\ \vdots \\ I_N \end{bmatrix} = \begin{bmatrix} j\omega M_{T1} I_T \\ j\omega M_{T2} I_T \\ \vdots \\ j\omega M_{TN} I_T \end{bmatrix} \quad (28)$$

$$\mathbf{Z}\mathbf{I} = j\omega I_T \mathbf{M}_T \quad (29)$$

$$\mathbf{I} = j\omega I_T \mathbf{Z}^{-1} \mathbf{M}_T \quad (30)$$

This $N \times N$ linear system can be solved via Eq. (30) to give the currents in each loop. The secondary EMF at the Rx coil will be the superposition of the EMF induced by each coil, represented by Eq. (31), which can then be used to represent the magnetic field ratio as Eq. (32).

$$\mathcal{E}_R^s = -j\omega \sum_{k=1}^N M_{kR} I_k e^{j\omega t} = -j\omega \mathbf{M}_R^\top \mathbf{I} e^{j\omega t} \quad (31)$$

$$\frac{H^s}{H^p} = \frac{\mathcal{E}_R^s}{\mathcal{E}_R^p} = \sum_{k=1}^N \frac{M_{kR} I_k}{M_{TR} I_T} = \frac{j\omega \mathbf{M}_R^\top \mathbf{Z}^{-1} \mathbf{M}_T}{M_{TR}} \quad (32)$$

This can be further simplified by assuming the mutual inductance between the loops is insignificant, which is the same as Eq. (33). We can also assume that the inductance and resistance for each loop are all the same. This allows us to express the impedance matrix as Eq. (34).

$$\omega M_{kl} \ll \sqrt{R_k^2 + \omega^2 L_k^2} \quad (33)$$

$$\mathbf{Z} \approx (R + j\omega L) \mathbb{I} \quad (34)$$

This simplification reduces Eq. (32) to Eq. (35), reducing the computational time complexity by about $O(N^3)$ by avoiding the matrix inversion.

$$\frac{H^s}{H^p} = \frac{j\omega \mathbf{M}_R^\top \mathbf{M}_T}{M_{TR}(R + j\omega L)} \quad (35)$$

To justify the assumption made in Eq. (33), the multi-loop model was implemented using both Eq. (32) and Eq. (35). The result is shown in Fig. 33. There is little difference between Fig. 33b and Fig. 33a, which indicates that the approximation does not significantly change the overall result. It is worth noting that the model without mutual inductance between the loops described by Eq. (35) was around 100 times faster to run for this example. This led us to use this model moving forward with our dataset creation and inversion pipeline.

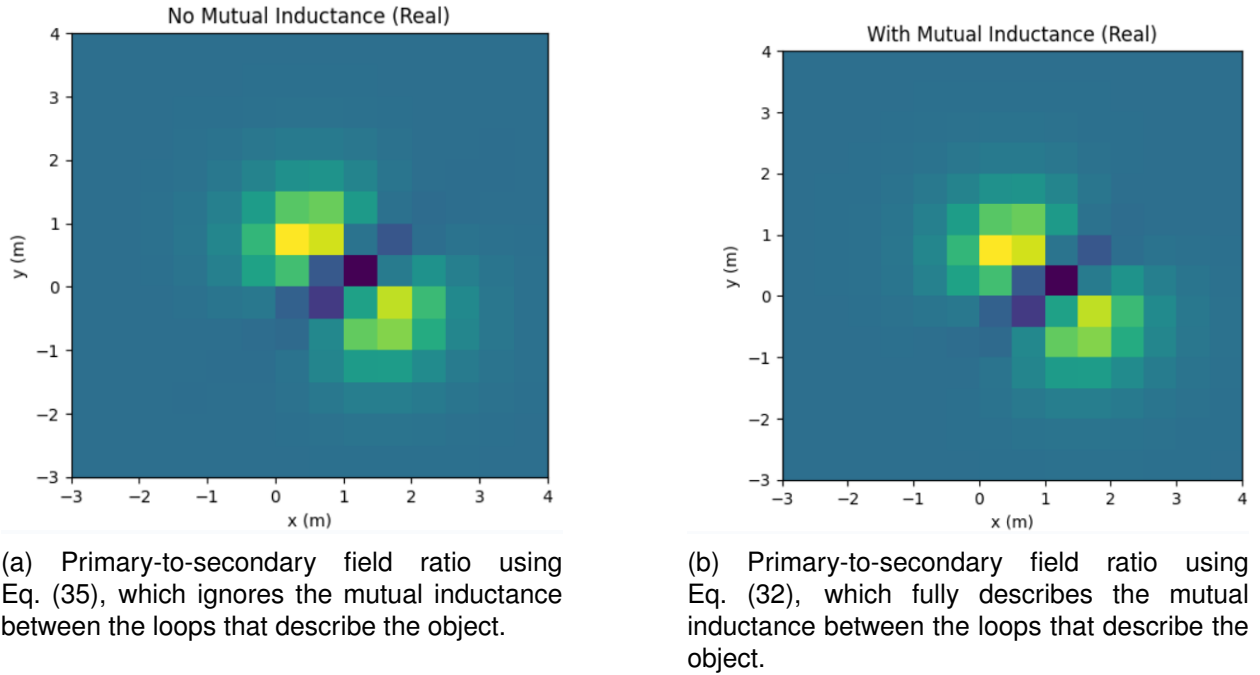


Figure 33: Comparison of the multi-loop approximation with (a) and without mutual inductance (b) between the loops.

F.3 Dependence on Conductivity

Finally, to relate the internal resistance and inductance of each loop to the conductivity and permeability of the object, known resistance and inductance formulas were used. The resistance was computed using Eq. (36) adapted for a thin-walled pipe with radius r , length l , and wall thickness δ , the skin depth characterized by Eq. (37). The resistance and inductance formulas can be adapted

for different shaped objects following a similar approach and used in the results from Appendix F.2.

$$R = \frac{l}{\sigma A} \quad (36)$$

$$\delta = \sqrt{\frac{1}{\pi \sigma \mu f}} \quad (37)$$

Assuming the current flows around the wall of the pipe, the total resistance of the pipe will be given by Eq. (38).

$$R = \frac{2\pi r}{\sigma \delta l} \quad (38)$$

This gives the equivalent resistance of the pipe. By breaking it into N loops of equal resistance R , we get Eq. (39).

$$R_{eq} = NR \quad (39)$$

This gives a resistance for each loop in the simulated model described by Eq. (40).

$$R = \frac{2\pi r N}{\sigma \delta l} \quad (40)$$

The inductance was computed by using Eq. (41). The magnetic field was assumed to be that of a solenoid (42), as it most closely matches the expected eddy currents of our pipe.

$$L = \frac{\Phi_B}{I} \quad (41)$$

$$B = \frac{\mu N I}{l} \quad (42)$$

The inductance for a single pipe can then be described by Eq. (43).

$$L = \frac{\mu \pi r^2 N}{l} \quad (43)$$

G Inversion Algorithm

This appendix summarizes the mathematical formulation and numerical techniques underlying the inversion of frequency-domain electromagnetic data, based on the algorithm implemented in Deidda et al. (2019).

G.1 Nonlinear Forward Model for Inversion

We model the subsurface as a stack of n horizontal layers, each with constant electrical conductivity σ_k , magnetic permeability μ_k and thickness d_k for $k = 1, \dots, n$. The thickness of the deepest

layer d_n is considered infinite. The two coils of the measuring device are at considered to be at height h above the ground and the inter-coil distance is ρ .

The depth-dependent response of the soil to an oscillating magnetic field is modeled using the following quantities:

Complex wavenumber:

$$u_k(\lambda) = \sqrt{\lambda^2 + i\sigma_k\mu_k\omega} \quad (44)$$

where λ ranges from zero to infinity, measuring the ratio between the depth below the ground and the inter-coil distance.

Characteristic admittance:

$$N_k(\lambda) = \frac{u_k(\lambda)}{i\mu_k\omega} \quad (45)$$

For $k = 0$, $N_0(\lambda) = \frac{\lambda}{i\mu_0\omega}$ where μ_0 is the permeability of free space.

Recursive surface admittance:

$$Y_k(\lambda) = N_k(\lambda) \cdot \frac{Y_{k+1}(\lambda) + N_k(\lambda) \tanh(d_k u_k(\lambda))}{N_k(\lambda) + Y_{k+1}(\lambda) \tanh(d_k u_k(\lambda))} \quad (46)$$

For $k = n$, the characteristic admittance and the surface admittance are assumed to coincide ($Y_n(\lambda) = N_n(\lambda)$).

Reflection factor:

$$R_{\omega,0}(\lambda) = \frac{N_0(\lambda) - Y_1(\lambda)}{N_0(\lambda) + Y_1(\lambda)} \quad (47)$$

where $Y_1(\lambda)$ is calculated using Eq.(46).

Hankel-transformed field ratio for Horizontal Coil Orientation:

$$M_H(\sigma, \mu; h, \omega, \rho) = -\rho^2 \int_0^\infty e^{-2h\lambda} R_{\omega,0}(\lambda) J_1(\rho\lambda) \lambda d\lambda \quad (48)$$

In Eq.(48), J_1 refers to the Bessel function of order 1.

The model output (M_H) are complex-valued:

- Real part (in-phase) is sensitive to magnetic permeability μ
- Imaginary part (quadrature) is sensitive to electrical conductivity σ

Since we are interested in the electrical conductivity, we are only interested in the imaginary component of M_H . From $Im(M_H)$, we can estimate the conductivity of the ground and this derived conductivity is called *apparent conductivity*. Eq.(49) shows the relationship between $Im(M_H)$ and apparent conductivity.

Apparent Conductivity:

$$\sigma_{\text{apparent}} = \frac{4}{2\pi\mu_0\omega\rho^2} \cdot \text{Im}(M_H) \quad (49)$$

G.2 Inverse Problem Formulation

Given a set of complex measurements $b \in \mathbb{C}^m$, the inverse problem is formulated as a nonlinear least-squares minimization:

$$\min_{\sigma, \mu \in \mathbb{R}^n} \frac{1}{2} \|b - M(\sigma, \mu)\|^2 \quad (50)$$

Eq.(50) is solved via the damped GaussNewton method. At each iteration, we linearize the residual function:

$$r(\sigma, \mu) = b - M(\sigma, \mu) \quad (51)$$

$$r(\sigma_k + s_k, \mu_k + t_k) \approx r(\sigma_k, \mu_k) + J_k \begin{bmatrix} s_k \\ t_k \end{bmatrix} \quad (52)$$

where $J_k \in \mathbb{C}^{m \times 2n}$ is the Jacobian matrix with respect to σ and μ .

To work with real-valued optimization, we stack the real and imaginary parts:

$$\tilde{r} = \begin{bmatrix} \beta \cdot \text{Re}(r) \\ \text{Im}(r) \end{bmatrix}, \quad \tilde{J} = \begin{bmatrix} \beta \cdot \text{Re}(J) \\ \text{Im}(J) \end{bmatrix} \quad (53)$$

The update is computed by solving:

$$q_k = -(\tilde{J}_k^\dagger \tilde{r}_k), \quad (\sigma_{k+1}, \mu_{k+1}) = (\sigma_k, \mu_k) + \alpha_k q_k \quad (54)$$

where \tilde{J}_k^\dagger is the pseudo-inverse and α_k is a damping factor (chosen by line search).

G.3 Regularization

The inversion problem described above is highly ill-posed, meaning that small perturbations (e.g., noise) in the measured data can lead to large, unstable variations in the computed solution. This instability is due to the Jacobian matrix \tilde{J}_k being ill-conditioned. To mitigate this issue, a regularization strategy is used into the GaussNewton framework to stabilize the inversion and incorporate prior information about the expected structure of the solution.

The regularized version of the linearized problem at iteration k takes the form:

$$\min_{q \in \mathbb{R}^{2n}} \|\tilde{J}_k q + \tilde{r}_k\|^2 + \lambda^2 \|Lq\|^2 \quad (55)$$

where q is the update vector containing increments for both conductivity and permeability parameters, L is a regularization matrix (e.g., discrete derivative operator) and λ is a regularization parameter.

Generalized Truncated SVD (TGSVD):

When prior knowledge (e.g., smoothness or decay) about the subsurface profile is available, the regularization matrix L is chosen accordingly, such as a discretized first- or second-derivative operator:

$$\min_{q \in S} \|Lq\|^2, \quad S = \left\{ q \in \mathbb{R}^{2n} : \tilde{J}_k^T \tilde{J}_k q = -\tilde{J}_k^T \tilde{r}_k \right\} \quad (56)$$

The effective solution $q^{(\ell)}$ is computed using only the most stable directions in the parameter space, where ℓ is the truncation index that determines how many components to retain.

Minimum Gradient Support (MGS):

In cases where the subsurface contains sharp or blocky features, smoothness-promoting regularization like TGSVD may oversmooth the result. Instead, the Minimum Gradient Support (MGS) regularization is used to promote sparsity in spatial gradients.

This is done by replacing the $\|Lq\|^2$ term with a nonlinear stabilizing functional:

$$S_\tau(q) = \sum_{i=1}^p \frac{(Lq)_i^2}{(Lq)_i^2 + \tau^2} \quad (57)$$

where $\tau > 0$ is a small parameter. As $\tau \rightarrow 0$, this expression tends to minimize the number of non-zero gradient components, effectively favoring blocky solutions.

Although the MGS approach seemed the most appropriate at first, due to the large magnitude of the UXO conductivity and its relatively small size in the model, this approach more noise and instability into the solution. Hence we decided to enforce "smoothness" rather than "spikiness" without our regularization.

G.4 Implementation Notes

- Choosing the right order of regularization parameter λ (or truncation index ℓ in TGSVD) is critical to achieving a good balance between fitting the data and avoiding overfitting to noise.
- The inversion framework supports simultaneous use of multiple heights, coil spacings, and operating frequencies. However, since our instrument performs a frequency sweep at a fixed height and coil spacing, the implemented code holds those two parameters constant while varying only the frequency.

- The Jacobian is computed analytically for accuracy and speed.

References

- Breiner, S. (1999). *Applications Manual For Portable Magnetometers*.
- Buccini, A. and Daz de Alba, P. (2021). A variational non-linear constrained model for the inversion of fdem data*. *Inverse Problems*, 38(1):014001.
- Deidda, G. P., Daz de Alba, P., Fenu, C., Lovicu, G., and Rodriguez, G. (2019). Fdemtools: a matlab package for fdem data inversion. *Numerical Algorithms*, 84(4):13131327.
- GeoSci Developers (2018). Circuit model for em induction. In *Electromagnetic Geophysics*. GeoSci Developers. Accessed: 2025-04-07.
- Naval Explosive Ordnance Disposal Technology Division (1996). *Unexploded Ordnance (UXO) Reference Manual*.
- Oldenburg, D., Jones, F., Heagy, L., Cockett, R., Astic, T., Devriese, S., Kang, S., and Capriotti, J. (2017). Basic principles. In *Geophysics for Practicing Geoscientists*. GeoSci Developers. Accessed: 2025-04-07.
- Simms, J. E., Larson, R. J., Murphy, W. L., and Butler, D. K. (2004). Guidelines for planning unexploded ordnance (uxo) detection surveys. *Geotechnical and Structures Laboratory*.
- Texas Instruments (2004). LM1875 20W Audio Power Amplifier Datasheet. Accessed: 2025-04-07.
- UNICEF (2009). Children and landmines: A deadly legacy. Retrieved from: https://web.archive.org/web/20090905185944/http://www.unicef.org/french/protection/files/Landmines_Factsheet_04_LTR_HD.pdf.